SEECCM III
3^{rd} South-East European Conference on Computational Mechanics-
an ECCOMAS and IACM Special Interest Conference
M. Papadrakakis, M. Kojic, I. Tuncer (eds.)
Kos Island, Greece, 12–14 June 2013

A PARALLEL FULLY COUPLED APPROACH FOR LARGE-SCALE FLUID-STRUCTURE INTERACTION PROBLEMS

Ali Eken[1] **and Mehmet Sahin**[2]

Faculty of Aeronautics and Astronautics
Astronautical Engineering Department
Istanbul Technical University, Maslak
Istanbul, 34469, TURKEY
[1] e-mail: ekena@itu.edu.tr
[2] e-mail: msahin@itu.edu.tr

Keywords: Fluid-Structure Interactions, Unstructured Finite Volume Method, Finite Element Method, Large Displacements, Large-Scale Computations; Monolithic Approaches.

Abstract. *A fully coupled numerical algorithm has been developed for the numerical simulation of large-scale fluid structure interaction problems. The incompressible Navier-Stokes equations are discretized using an Arbitrary Lagrangian-Eulerian (ALE) formulation based on the side-centered unstructured finite volume method. The side-centered arrangement of the primitive variables leads to a stable numerical scheme and it does not require any ad-hoc modifications in order to enhance the pressure-velocity coupling. The continuity equation is satisfied within each element exactly and the summation of the continuity equations can be exactly reduced to the domain boundary, which is important for the global mass conservation. A special attention is also given to satisfy the discrete geometric conservation law (DGCL). The nonlinear elasticity equations are discretized within the structure domain using the Galerkin finite element method. The structural behaviour of solid domain is governed by the the constitutive laws for the nonlinear Saint Venant-Kirchhoff material. The resulting algebraic nonlinear equations are solved in a fully coupled form using the restricted additive Schwarz method with the flexible GMRES(m) algorithm. The implementation of the fully coupled preconditioned iterative solvers is based on the PETSc library for improving the efficiency of the parallel code. The present numerical algorithm is validated for a Newtonian fluid interacting with an elastic rectangular bar behind a circular cylinder, a three-dimensional elastic solid confined in a rectangular channel and a pulsatile flow in a flexible tube, which mimics the case of pulsatile blood flow through elastic arteries.*

1 INTRODUCTION

The fluid-structure interaction (FSI) problem is probably one of the most addressed multi-physics problems in the literature, not only for its numerous applications in engineering and biomechanics, but also for the computational challenges involved in its numerical modeling and simulation. The FSI problem is mainly characterized by the mutual interaction between a movable or deformable structure with an internal or surrounding fluid flow. Typical examples in engineering applications involve aeroelastic phenomena like flutter of aircraft wings [1, 2] or turbine blades [3] and tail buffeting [4], inflation of parachutes [5] or airbags [6], design of sails [7] or tent structures [8], structural effect of strong wind on bridges [9] and tall buildings [10], and many others. On the other hand, much of the work in biomedical applications include blood flow in the veins and arteries [11], dynamics of heart valves [12, 13], deformations and aggregations of blood cells [14, 15]. Accurate prediction of fluid-structure interactions is crucial for many engineering structures in order to avoid potential aeroelastic/hydroelastic instabilities, which may cause catastrophic failures of the structure. A typical example for such a case is wing flutter, which occurs as a result of exchange of energy between different modes of the structure because of fluid-structure interactions leading to large amplitudes and stresses, which can tear an airframe apart.

There are mainly two approaches for the modeling of fluid-structure interaction problems: partitioned (segregated) [16, 17, 18] or fully coupled (monolithic) [19, 20, 21] methods. In the partitioned approach, separate solvers are used for the fluid and structure subproblems. The main advantage of the partitioned approach is the ability to reuse existing solvers, which allows the application of different, possibly more efficient computational methods specifically developed for either the fluid or the structure subproblems. Both explicit or implicit methods can be used in order to couple the fluid and structure solvers in partitioned procedures. In explicit partitioned methods, which are also known as loosely or weakly coupled methods, typically a fixed point (Picard) iteration is employed to obtain a coupled solution. Although the implementation of this method is relatively easy, it does, however, suffer some serious drawbacks. The fixed point iterations tend to converge slowly if at all, and the iterations may diverge in the presence of strong fluid-solid interactions due to a comparable fluid-to-solid density ratio, which is encountered frequently in FSI problems in biomechanics [22, 23]. In addition, weakly coupled partitioned methods can not satisfy the incompressibility constraint of the fluid [24] during standard alternating FSI iterations when the fluid domain is entirely enclosed by Dirichlet boundary conditions. For strong coupling in partitioned procedures, on the contrary, several fluid and structure computations are performed in a single time-step until a satisfactory convergence tolerance is reached. This approach, however requires costly sub-iterations, and the sub-iteration convergence may not be guaranteed. In a fully coupled approach, the fluid and structure equations are discretised and solved simultaneously as a single equation system for the entire problem. However, this requires an efficient numerical technique for the solution of a large system of coupled nonlinear algebraic equations, which poses the major challenge of monolithic FSI approaches, especially in large scale problems. Although monolithic solver are believed to be too expensive for use in large-scale problems, more recent studies [25, 26] demonstrate that monolithic solvers are competitive even in test cases with very weak FSI, where their segregated counterparts do not suffer from any convergence problems. In this context, Muddle et al. [21] presented a block preconditioner for the efficient solution of the linear systems by Krylov subspace solvers. Behr and Tezduyar [27] presented solution strategies for large scale flow simulations and Johnson and Tezduyar [28] proposed mesh update strategies in parallel computations. Gee et al. [20] applied an algebraic multigrid technique to the entire fluidstructure interaction system of equations. Barker and Cai [29] developed a scalable parallel finite element solver for the simulation of blood flow in compliant arteries using scalable Newton-Krylov algorithms with an overlapping restricted additive Schwarz method.

One of the most well-known methods used to capture the interaction between structure and fluid is the Arbitrary Lagrangian Eulerian (ALE) method as described in Hirt el al. [30]. In the ALE method, the mesh follows the interface between the fluid and solid boundary and the governing equations are discretized on a moving mesh. This differs from the standard Eulerian formulation in a way that the mesh movement has to fulfill special conditions in order to maintain the accuracy and the stability of the time integration scheme. This condition is satisfied by the enforcement of the so-called geometric conservation law (GCL) as coined by Thomas and Lombard [31]. The ALE approach was subsequently adopted within the finite element context to solve free surface problems of incompressible viscous fluid flow [32]. In the case of an FSI problem, the deformable fluid-structure interface is taken into account and the fluid points at the fluid-solid interface are moved in a Lagrangian way [33]. This article presents a new numerical algorithm based on the ALE formulation for a fully coupled solution of the large-scale FSI problems where the fluid is modelled by the incompressible Navier-Stokes equations and the structure is modeled by the St. Venant-Kirchhoff model. The governing equations of the fluid domain are discretized using an Arbitrary Lagrangian-Eulerian (ALE) formulation based on the side-centered unstructured finite volume method where the velocity vector components are defined at the mid-point of each cell face while the pressure is defined at the element centroid. The present arrangement of the primitive variables leads to a stable numerical scheme and it does not require any *ad-hoc* modifications in order to enhance the pressure-velocity coupling. This approach was initially used by Hwang [34] and Rida *et al.* [35] for the solution of the incompressible Navier-Stokes equations on unstructured triangular meshes. The most appealing feature of the present finite volume approach is that it leads to the classical five-point Laplace operator for the pressure Poisson equation as in the classical MAC scheme [36] which is very important for the efficient solution of the large-scale FSI problems. Because, numerical simulations of FSI problems in general require large computational resources, and it is typically the fluid subproblem that requires the most computational resources in the coupled system [37]. In the present work, a special attention will be given to satisfy the continuity equation exactly within each element and the summation of the continuity equations can be exactly reduced to the domain boundary, which is important for the global mass conservation. The mesh deformation within the fluid domain is achieved by using an algebraic approach based on the minimum distance function at each time level while avoiding re-meshing in order to enhance numerical robustness. The deformation of the solid domain is governed by the constitutive laws for the nonlinear Saint Venant-Kirchhoff material and the classical Galerkin finite element is used to discretise the governing equations in a Lagrangian frame. Newmark [38] type generalized-α method [39] is employed to integrate in time the solid dynamic equilibrium equation.

The remainder of this paper is organized as follows: Section 2 provides some details on the present FSI method. The mathematical and numerical formulations of the ALE based unstructured finite volume method for the fluid and the finite element method for the structure are given in detail. In Section 3, the proposed method is validated for three reference FSI benchmark problems: A steady Newtonian fluid interacting with an elastic bar behind a cylinder, a three-dimensional elastic solid in a steady channel flow and a pulsatile flow in a flexible tube, which mimics the case of pulsatile blood flow through elastic arteries. Concluding remarks are provided in Section 4.

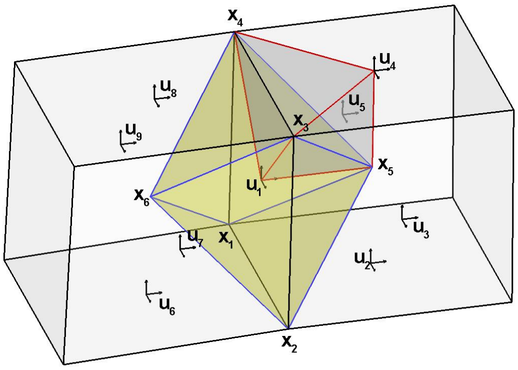

Figure 1: Three-dimensional unstructured mesh with a dual control volume for the velocity components.

2 MATHEMATICAL and NUMERICAL FORMULATION

2.1 Fluid model

The integral form of the incompressible NavierStokes equations that govern the motion of an arbitrary moving control volume $\Omega(t)$ with boundary $\partial\Omega(t)$ can be written in the Cartesian coordinate system in dimensionless form as follows: the momentum equations

$$Re\int_{\Omega_d}\frac{\partial\mathbf{u}}{\partial t}dV+Re\oint_{\partial\Omega_d}\left[\mathbf{n}\cdot(\mathbf{u}-\dot{\mathbf{x}})\right]\mathbf{u}dS+\oint_{\partial\Omega_d}\mathbf{n}pdS=\oint_{\partial\Omega_d}\mathbf{n}\cdot\nabla\mathbf{u}dS \tag{1}$$

the continuity equation

$$-\oint_{\partial\Omega_e}\mathbf{n}\cdot\mathbf{u}\,dS=0 \tag{2}$$

In these equations, V is the control volume, S is the control volume surface area, $\mathbf{n}$ represents the outward normal vector, $\mathbf{u}$ represents the local fluid velocity vector, $\dot{\mathbf{x}}$ represents the grid velocity (the velocity vector of the control volume surface), p is the pressure and Re is the dimensionless Reynolds number. Figure 1 illustrates typical two neighboring hexahedral elements with a dual finite volume constructed by connecting the element centroids to the common vertices shared by the both hexahedral elements. The local fluid velocity vector components are defined at the mid-point of each face.

2.2 Solid model

The structural behaviour of solid domain is governed by the following conservation of momentum in the Lagrangian framework where the material derivative becomes a partial derivative with respect to time

$$\rho\frac{\partial^2\mathbf{d}}{\partial \mathrm{t}^2}=\nabla\cdot\boldsymbol{\sigma}_s+\rho\mathbf{b} \tag{3}$$

where ρ is the solid material density, $\mathbf{d}$ is the displacement vector, σ_s is the Cauchy stress tensor and $\mathbf{b}$ is the body forces. The material is defined by the Cauchy stress tensor using the following constitutive law for the St. Venant-Kirchhoff material:

$$\begin{aligned} \mathbf{S} &= J\mathbf{F}^{-1}\sigma_s\mathbf{F}^{-\top} && (4)\\ \mathbf{F} &= (\mathbf{I}+\nabla\mathbf{d}) && (5)\\ \mathbf{E} &= \frac{1}{2}(\mathbf{F}^{\top}\mathbf{F}-\mathbf{I}) && (6)\\ \mathbf{S} &= \lambda\text{trace}(\mathbf{E})\mathbf{I}+2\mu\mathbf{E} && (7)\\ \mathbf{\Pi} &= \mathbf{FS} && (8) \end{aligned}$$

where $\mathbf{S}$ is the second Piola-Kirchhoff stress tensor, $\mathbf{F}$ is the deformation gradient tensor, $J = det(\mathbf{F})$ is the deformation gradients determinant, $\mathbf{E}$ is the Green-Lagrange strain tensor, $\mathbf{\Pi}$ is the non-symmetric first Piola-Kirchhoff stress tensor and λ and μ are the material Lame's constants. Then the equation of motion with respect to the initial configuration is given by

$$\rho_0\frac{\partial^2\mathbf{d}}{\partial \mathrm{t}^2} = \nabla\cdot\mathbf{\Pi}+\rho_0\mathbf{b} \tag{9}$$

where ρ_0 is the solid material density per unit undeformed volume.

2.3 Interface conditions

A main requirement for the coupling schemes is to fulfill two coupling conditions: the kinematic and the dynamic continuity across the fluid-solid interface at all times. The kinematic boundary conditions on the fluid-structue interface is driven by requiring continuity of the velocity

$$\mathbf{u} = \dot{\mathbf{d}} \tag{10}$$

while the dynamic condition means that the following equilibrium equation holds for the surface traction at the common fluid-structure interaction boundary

$$\sigma_s\mathbf{n}_s = -\sigma_f\mathbf{n}_f \tag{11}$$

where $\mathbf{n}_s$ and $\mathbf{n}_f$ denote the outward-pointing unit normal on the fluid-structure boundary, viewed from the structure and fluid domains, respectively. Here, σ_s represents the Cauchy stress tensor of the structural field and σ_f is the stress tensors in the case of an incompressible Newtonian fluid. The constitutive relation for the fluid stress tensor is given by

$$\sigma_f = -p\mathbf{I}+\mu(\nabla\mathbf{u}+\nabla\mathbf{u}^{\top}) \tag{12}$$

where μ is the fluid dynamic viscosity.

2.4 Numerical discretization of ALE formulation for fluid domain

The momentum equations along the $x-$, $y-$ and $z-$directions are discretized over the dual finite volume shown in Figure 1 and the dual volume involves only the right and left elements that share the common face where the components of the velocity vector are discretized. The discrete contribution from the right cell shown in Figure 1 is given below for each term of the momentum equation along the $x-$direction. The time derivative

$$Re\left[\frac{3u_1^{n+1}}{4\Delta t}+\frac{\sum_i u_i^{n+1}}{6\cdot 4\Delta t}\right]V_{12345} - Re\left[\frac{3u_1^{n}}{4\Delta t}+\frac{\sum_i u_i^{n}}{6\cdot 4\Delta t}\right]V_{12345} \quad \text{with} \quad i=1,2,3,4,5,10 \tag{13}$$

The convective term due to fluid motion

$$
\begin{aligned}
&\frac{1}{2}Re\left[\mathbf{u}_{125}^{n}\cdot\mathbf{A}_{125}^{n+1}\right]u_{125}^{n+1}+\tfrac{1}{2}Re\left[\mathbf{u}_{125}^{n}\cdot\mathbf{A}_{125}^{n}\right]u_{125}^{n+1}\\
+&\frac{1}{2}Re\left[\mathbf{u}_{235}^{n}\cdot\mathbf{A}_{235}^{n+1}\right]u_{235}^{n+1}+\tfrac{1}{2}Re\left[\mathbf{u}_{235}^{n}\cdot\mathbf{A}_{235}^{n}\right]u_{235}^{n+1}\\
+&\frac{1}{2}Re\left[\mathbf{u}_{345}^{n}\cdot\mathbf{A}_{345}^{n+1}\right]u_{345}^{n+1}+\tfrac{1}{2}Re\left[\mathbf{u}_{345}^{n}\cdot\mathbf{A}_{345}^{n}\right]u_{345}^{n+1}\\
+&\frac{1}{2}Re\left[\mathbf{u}_{415}^{n}\cdot\mathbf{A}_{415}^{n+1}\right]u_{415}^{n+1}+\tfrac{1}{2}Re\left[\mathbf{u}_{415}^{n}\cdot\mathbf{A}_{415}^{n}\right]u_{415}^{n+1}
\end{aligned}
\tag{14}
$$

The convective term due to mesh motion

$$
\begin{aligned}
-&\frac{1}{2}Re\left[\dot{\mathbf{x}}_{125}^{n+1}\cdot\mathbf{A}_{125}^{n+1}\right]u_{125}^{n}-\tfrac{1}{2}Re\left[\dot{\mathbf{x}}_{125}^{n+1}\cdot\mathbf{A}_{125}^{n}\right]u_{125}^{n}\\
-&\frac{1}{2}Re\left[\dot{\mathbf{x}}_{235}^{n+1}\cdot\mathbf{A}_{235}^{n+1}\right]u_{235}^{n}-\tfrac{1}{2}Re\left[\dot{\mathbf{x}}_{235}^{n+1}\cdot\mathbf{A}_{235}^{n}\right]u_{235}^{n}\\
-&\frac{1}{2}Re\left[\dot{\mathbf{x}}_{345}^{n+1}\cdot\mathbf{A}_{345}^{n+1}\right]u_{345}^{n}-\tfrac{1}{2}Re\left[\dot{\mathbf{x}}_{345}^{n+1}\cdot\mathbf{A}_{345}^{n}\right]u_{345}^{n}\\
-&\frac{1}{2}Re\left[\dot{\mathbf{x}}_{415}^{n+1}\cdot\mathbf{A}_{415}^{n+1}\right]u_{415}^{n}-\tfrac{1}{2}Re\left[\dot{\mathbf{x}}_{415}^{n+1}\cdot\mathbf{A}_{415}^{n}\right]u_{415}^{n}
\end{aligned}
\tag{15}
$$

The pressure term

$$
\begin{aligned}
&\left[\frac{p_1+p_2+p_5}{3}\right]^{n+1}\mathbf{A}_{125}^{n+1}\cdot\mathbf{i}+\left[\frac{p_2+p_3+p_5}{3}\right]^{n+1}\mathbf{A}_{235}^{n+1}\cdot\mathbf{i}\\
+&\left[\frac{p_3+p_4+p_5}{3}\right]^{n+1}\mathbf{A}_{345}^{n+1}\cdot\mathbf{i}+\left[\frac{p_4+p_1+p_5}{3}\right]^{n+1}\mathbf{A}_{415}^{n+1}\cdot\mathbf{i}
\end{aligned}
\tag{16}
$$

The viscous term

$$
\begin{aligned}
-&\left[\left(\frac{\partial u}{\partial x}\right)_{125}^{n+1}\mathbf{A}_{125}^{n+1}\cdot\mathbf{i}+\left(\frac{\partial u}{\partial y}\right)_{125}^{n+1}\mathbf{A}_{125}^{n+1}\cdot\mathbf{j}+\left(\frac{\partial u}{\partial z}\right)_{125}^{n+1}\mathbf{A}_{125}^{n+1}\cdot\mathbf{k}\right]\\
-&\left[\left(\frac{\partial u}{\partial x}\right)_{235}^{n+1}\mathbf{A}_{235}^{n+1}\cdot\mathbf{i}+\left(\frac{\partial u}{\partial y}\right)_{235}^{n+1}\mathbf{A}_{235}^{n+1}\cdot\mathbf{j}+\left(\frac{\partial u}{\partial z}\right)_{235}^{n+1}\mathbf{A}_{235}^{n+1}\cdot\mathbf{k}\right]\\
-&\left[\left(\frac{\partial u}{\partial x}\right)_{345}^{n+1}\mathbf{A}_{345}^{n+1}\cdot\mathbf{i}+\left(\frac{\partial u}{\partial y}\right)_{345}^{n+1}\mathbf{A}_{345}^{n+1}\cdot\mathbf{j}+\left(\frac{\partial u}{\partial z}\right)_{345}^{n+1}\mathbf{A}_{345}^{n+1}\cdot\mathbf{k}\right]\\
-&\left[\left(\frac{\partial u}{\partial x}\right)_{415}^{n+1}\mathbf{A}_{415}^{n+1}\cdot\mathbf{i}+\left(\frac{\partial u}{\partial y}\right)_{415}^{n+1}\mathbf{A}_{415}^{n+1}\cdot\mathbf{j}+\left(\frac{\partial u}{\partial z}\right)_{415}^{n+1}\mathbf{A}_{415}^{n+1}\cdot\mathbf{k}\right]
\end{aligned}
\tag{17}
$$

where V_{12345} is the volume of the pyramid between the points $\mathbf{x}_1$, $\mathbf{x}_2$, $\mathbf{x}_3$, $\mathbf{x}_4$ and $\mathbf{x}_5$ shown in Figure 1, $\mathbf{A}_{125}$, $\mathbf{A}_{235}$, $\mathbf{A}_{345}$ and $\mathbf{A}_{415}$ are the area vectors of the dual volume triangular surfaces, Δt is the time step, the values $\mathbf{u}_{125}$, $\mathbf{u}_{235}$, $\mathbf{u}_{345}$ and $\mathbf{u}_{415}$ are the velocity vectors defined at the mid-point of each dual volume area and p_1, p_2, p_3, p_4 and p_5 are the pressure values at the points

$\mathbf{x}_1$, $\mathbf{x}_2$, $\mathbf{x}_3$, $\mathbf{x}_4$ and $\mathbf{x}_5$, respectively. However, the pressure values at $\mathbf{x}_1$, $\mathbf{x}_2$, $\mathbf{x}_3$ and $\mathbf{x}_4$ are not known. To compute the pressure at $\mathbf{x}_1$, as an example, a second-order Taylor series expansion can be written as

$$p_i = p_1 + \frac{\partial p}{\partial x}\,|_{\mathbf{x}=\mathbf{x}_1}\,(x_i - x_1) + \frac{\partial p}{\partial y}\,|_{\mathbf{x}=\mathbf{x}_1}\,(y_i - y_1) + \frac{\partial p}{\partial z}\,|_{\mathbf{x}=\mathbf{x}_1}\,(z_i - z_1) \tag{18}$$

where i represents the neighboring hexahedral elements connected to the $\mathbf{x}_1$ point. This overdetermined system of linear equations may be solved in a least square sense using the normal equation approach, in which both sides are multiplied by the transpose. The modified system is solved using the singular value decomposition provided by the Intel Math Kernel Library in order to avoid the numerical difficulties associated with solving linear systems with near rank deficiency. The velocity components are also computed at the points $\mathbf{x}_1$, $\mathbf{x}_2$, $\mathbf{x}_3$ and $\mathbf{x}_4$ in a similar manner. The velocity vector gradient components defined at the mid-point of each dual volume faces are computed by the use of the Green-Gauss theorem:

$$\nabla u = \frac{\partial u}{\partial x}\mathbf{i} + \frac{\partial u}{\partial y}\mathbf{j} + \frac{\partial u}{\partial z}\mathbf{k} = \frac{1}{V_C}\oint_{\partial\Omega_c} u d\mathbf{A} \tag{19}$$

where V_C covolume consists two tetrahedral elements that share the same dual volume surface area and have their fourth vertices at the upwind and downwind velocity locations of the same dual volume surface area (for $\mathbf{A}_{125}$, the locations where $\mathbf{u}_1$ and $\mathbf{u}_2$ are defined). The right-hand side of the equations (19) is evaluated using the mid-point rule on each of the covolume faces. It should be noted that for the present finite-volume surface integrals involve only triangular planar surfaces for the momentum equations. The convective velocity vector components u_{125}, u_{235}, u_{345} and u_{415} are computed using the least square interpolations [40, 41]. As an example,

$$u_{125} = \beta\left[u_1 + \nabla u_1 \mathbf{r}_1\right] + (1-\beta)\left[u_2 + \nabla u_2 \mathbf{r}_2\right] \tag{20}$$

where β is a weight factor determining the type of convection scheme used, ∇u_1 and ∇u_2 are the gradients of velocity components where the u_1 and u_2 velocity components are defined and $\mathbf{r}_1$ and $\mathbf{r}_2$ are the distance vectors from the mid-point of the dual volume surface to the locations where the gradients of velocity components are computed. For evaluating the gradient terms, ∇u_1 and ∇u_2, a least square procedure is used in which the velocity data is assumed to behave linearly. In order to satisfy the geometric conservation law (GCL) at the discrete level, the grid velocity components are computed through the use of the first-order backward differences.

$$\dot{\mathbf{x}}^{n+1} = \frac{\mathbf{x}^{n+1} - \mathbf{x}^{n}}{\Delta t} \tag{21}$$

This will ensure that the numerical scheme preserve a uniform flow solution exactly independent of the mesh motion. In comparison to the staggered methods, the use of the both velocity components significantly simplifies the discretization of the governing equations as well as the implementation of physical boundary conditions. The discretization of the momentum equation along the $y-$ and $z-$direction follows very closely the ideas presented here. The continuity equation (2) is integrated within each hexahedral elements and evaluated using the mid-point rule on each of the element faces

$$-\sum_{i=1}^{6}\left[u^{n+1}A_x\right]_i + \left[v^{n+1}A_y\right]_i + \left[w^{n+1}A_z\right]_i = 0 \tag{22}$$

where $\mathbf{A} = A_x\mathbf{i} + A_y\mathbf{j} + A_z\mathbf{k}$ is the hexahedral element surface area vector and u, v and w are the velocity vector components defined at the mid-point of each hexahedral element face. The discretization of above equations leads to a saddle point problem of the form:

$$\begin{bmatrix} A_{11} & 0 & 0 & A_{14} \\ 0 & A_{22} & 0 & A_{24} \\ 0 & 0 & A_{33} & A_{34} \\ A_{41} & A_{42} & A_{43} & 0 \end{bmatrix} \begin{bmatrix} u \\ v \\ w \\ p \end{bmatrix} = \begin{bmatrix} b_1 \\ b_2 \\ b_3 \\ 0 \end{bmatrix} \tag{23}$$

where, A_{11}, A_{22} and A_{33} are the convection diffusion operators, $(A_{14}, A_{24}, A_{34})^\top$ is the pressure gradient operator and (A_{41}, A_{42}, A_{43}) is the divergence operator. It should also be noted that on an uniform Cartesian mesh the multiplication of the matrices $B_{41}B_{14} + B_{42}B_{24} + B_{43}B_{34}$ gives the classical five-point Laplace operator as in the MAC scheme [36] which is extremely important for the efficient implementation of the present preconditioned iterative solvers.

2.5 Galerkin finite element discretization for solid domain

The weak form of the equations can be obtained by multiplying the equation (9) by the test functions, and integrating over the volume of the element as follows

$$\int_{\Omega_s} N_i \rho \frac{\partial^2 \mathbf{d}}{\partial t^2} dV_0 = \int_{\Omega_s} N_i \left(\nabla \cdot \mathbf{\Pi} + \rho \mathbf{b}\right) dV_0 \tag{24}$$

Integrating by parts one has

$$\int_{\Omega_s} N_i \rho \frac{\partial^2 \mathbf{d}}{\partial t^2} dV_0 = \int_{\Omega_s} \nabla \cdot \left(N_i \mathbf{\Pi}\right) dV_0 - \int_{\Omega_s} \mathbf{\Pi} \nabla N_i dV_0 + \int_{\Omega_s} N_i \rho \mathbf{b} dV_0 \tag{25}$$

The first term can be related to a surface integral by the divergence theorem over the closed surface of the element, and the weak form in tensor notation can be obtained as

$$\int_{\Omega_s} N_i \rho \frac{\partial^2 \mathbf{d}}{\partial t^2} dV_0 = \oint_{\partial\Omega_s} \left(N_i \mathbf{\Pi}\right) \mathbf{n} dS_0 - \int_{\Omega_s} \mathbf{\Pi} \nabla N_i dV_0 + \int_{\Omega_s} N_i \rho \mathbf{b} dV_0 \tag{26}$$

The displacements at any point in the isoparametric hexahedral element are approximated by a linear combination of the displacements at the nodal points of the element

$$\begin{Bmatrix} d_x \\ d_y \\ d_z \end{Bmatrix} = \begin{bmatrix} N_1 & 0 & 0 & N_2 & 0 & 0 & N_3 & 0 & 0 & \cdots & N_8 & 0 & 0 \\ 0 & N_1 & 0 & 0 & N_2 & 0 & 0 & N_3 & 0 & \cdots & 0 & N_8 & 0 \\ 0 & 0 & N_1 & 0 & 0 & N_2 & 0 & 0 & N_3 & \cdots & 0 & 0 & N_8 \end{bmatrix} \begin{Bmatrix} d_{x1} \\ d_{y1} \\ d_{z1} \\ \vdots \\ d_{x8} \\ d_{y8} \\ d_{z8} \end{Bmatrix} = \mathbf{Nd} \tag{27}$$

The stiffness matrix for the hexahedral element is obtained from the discretization of the third integral term of the weak form of the equations (26).

$$\int_{\Omega_s} \mathbf{\Pi} \nabla N_i dV_0 = \int_{\Omega_s} \boldsymbol{F}\boldsymbol{S} \nabla N_i dV_0 = \int_{\Omega_s} (\mathbf{I} + \nabla \mathbf{d}) \boldsymbol{S} \nabla N_i dV_0 \tag{28}$$

The operation of the second Piola-Kirchhoff stress tensor on ∇N_i can explicitly given in matrix notation as

$$\boldsymbol{S}\,\nabla N_i = [B_i]^\top \{S\} \tag{29}$$

The integral can be obtained, at this stage, as

$$\int_{\Omega_s} \mathbf{\Pi}\nabla N_i dV_0 \;=\; \int_{\Omega_s} (\mathbf{I}+\nabla\mathbf{d})[B_i]^\top \{S\}\, dV_0 \tag{30}$$

where

$$(\mathbf{I}+\nabla\mathbf{d})[B_i]^\top = [B_i]^\top + \nabla\mathbf{d}[B_i]^\top = [B_i]^\top + [B_i]^\top_{NL} \tag{31}$$

The second Piola-Kirchhoff stress tensor can be written as

$$\left\{\begin{array}{c} S_{xx} \\ S_{yy} \\ S_{zz} \\ S_{xy} \\ S_{xz} \\ S_{yz} \end{array}\right\} = \underbrace{\left[\begin{array}{cccccc} \lambda+2\mu & \lambda & \lambda & 0 & 0 & 0 \\ \lambda & \lambda+2\mu & \lambda & 0 & 0 & 0 \\ \lambda & \lambda & \lambda+2\mu & 0 & 0 & 0 \\ 0 & 0 & 0 & \mu & 0 & 0 \\ 0 & 0 & 0 & 0 & \mu & 0 \\ 0 & 0 & 0 & 0 & 0 & \mu \end{array}\right]}_{\mathbf{C}} \left\{\begin{array}{c} E_{xx} \\ E_{yy} \\ E_{zz} \\ 2E_{xy} \\ 2E_{xz} \\ 2E_{yz} \end{array}\right\} \tag{32}$$

where the Green-St. Venant strain tensor can be obtained in vector form using the definition given in (5) and (6). Defining the displacement field in terms of the nodal displacements using (27), the the Green-St. Venant strain tensor in vector form can be obtained as

$$\{E\} = [\mathbf{B} + \frac{1}{2}\mathbf{B}_{NL}]\{\mathbf{d}\} \tag{33}$$

Hence, the element stiffness matrix can be calculated as

$$\mathbf{K}_{(e)} \;=\; \int_{\Omega_s} (\mathbf{B}+\mathbf{B}_{NL})^\top \mathbf{C}(\mathbf{B}+\frac{1}{2}\mathbf{B}_{NL})dV_0 \tag{34}$$

It should be noted that we do not use the Newton's method here. The element mass matrix can be obtained from the inertial term in the equation (26) by substituting the displacements equation (27) one has

$$\mathbf{M}_{(e)} = \int_{\Omega_s} \rho\mathbf{N}^T\mathbf{N}dV_0 \tag{35}$$

Finally, the boundary loads are imposed on the face of the surface elements by the surface integral term given in the equation (26)

$$\oint_{\partial\Omega_s} N_i \left[\begin{array}{ccc} \Pi_{xx} & \Pi_{xy} & \Pi_{xz} \\ \Pi_{yx} & \Pi_{yy} & \Pi_{yz} \\ \Pi_{zx} & \Pi_{zy} & \Pi_{zz} \end{array}\right] \left\{\begin{array}{c} n_x \\ n_y \\ n_z \end{array}\right\} dS_0 = \oint_{\partial\Omega_s} N_i \left[\begin{array}{ccc} \sigma_{xx} & \sigma_{xy} & \sigma_{xz} \\ \sigma_{yx} & \sigma_{yy} & \sigma_{yz} \\ \sigma_{zx} & \sigma_{zy} & \sigma_{zz} \end{array}\right]_s \left\{\begin{array}{c} \hat{n}_x \\ \hat{n}_y \\ \hat{n}_z \end{array}\right\} dS \tag{36}$$

where $\hat{\mathbf{n}}$ is the surface normal vector given in the deformed solid domain

$$\hat{\mathbf{n}} = \hat{n}_x\mathbf{i} + \hat{n}_y\mathbf{j} + \hat{n}_z\mathbf{k} \tag{37}$$

Then the following equilibrium equation is applied at the common fluid-structure interaction boundary

$$\sigma_s\hat{\mathbf{n}}_s = -\sigma_f\hat{\mathbf{n}}_f \tag{38}$$

Upon assembly of the element matrices the following dynamic system of equations can be obtained for the structure.

$$\mathbf{M}\ddot{\mathbf{d}} + \mathbf{R}(\mathbf{d}) = \mathbf{F} \tag{39}$$

where $\mathbf{M}$, $\mathbf{R}(\mathbf{d})$ and $\mathbf{F}$ are the global mass matrix, nonlinear residual due to material stiffness and load vector respectively, and $\mathbf{d}$ is the vector of global displacements. In the present approach the system given in (40) is solved using the generalized$-\alpha$ method of Chung and Hulbert [39].

2.6 Generalized$-\alpha$ method

Upon assembly of the element matrices the following dynamic system of equations can be obtained for the structure.

$$\mathbf{M}\ddot{\mathbf{d}} + \mathbf{R}(\mathbf{d}) = \mathbf{F} \tag{40}$$

where $\mathbf{M}$, $\mathbf{R}(\mathbf{d})$ and $\mathbf{F}$ are the global mass matrix, nonlinear residual due to material stiffness and load vector respectively, and $\mathbf{d}$ is the vector of global displacements. In the present approach the system given in (40) is solved using the generalized$-\alpha$ method of Chung and Hulbert [39]. The generalized$-\alpha$ method is an implicit, onestep time integration scheme based on Newmark like approximations [38] in the time domain and the modified form of the equation of motion becomes

$$\mathbf{M}\ddot{\mathbf{d}}_\alpha + \mathbf{R}(\mathbf{d}_\alpha) = \mathbf{F}_\alpha \tag{41}$$

The method relies on the following interpolations that relate positions, velocities, and accelerations:

$$\begin{aligned} \mathbf{d}_{n+1} &= \mathbf{d}_n + \Delta t\dot{\mathbf{d}}_n + \frac{\Delta t^2}{2}\left[(1-2\beta)\,\ddot{\mathbf{d}}_n + 2\beta\ddot{\mathbf{d}}_{n+1}\right] && (42)\\ \dot{\mathbf{d}}_{n+1} &= \dot{\mathbf{d}}_n + (1-\gamma)\,\Delta t\ddot{\mathbf{d}}_n + \gamma\Delta t\ddot{\mathbf{d}}_{n+1} && (43) \end{aligned}$$

The acceleration term is solved from equations (42) and then inserted into the equation (43). The modified equations can be written as

$$\begin{aligned} \ddot{\mathbf{d}}_{n+1} &= \frac{1}{\beta\Delta t^2}\left(\mathbf{d}_{n+1} - \mathbf{d}_n\right) - \frac{1}{\beta\Delta t}\dot{\mathbf{d}}_n - \left(\frac{1}{2\beta} - 1\right)\ddot{\mathbf{d}}_n && (44)\\ \dot{\mathbf{d}}_{n+1} &= \frac{\gamma}{\beta\Delta t}\left(\mathbf{d}_{n+1} - \mathbf{d}_n\right) - \left(\frac{\gamma}{\beta} - 1\right)\dot{\mathbf{d}}_n - \left(\frac{\gamma}{2\beta} - 1\right)\Delta t\ddot{\mathbf{d}}_n && (45) \end{aligned}$$

where β and γ are the Newmark parameters. Subscripts α denote evaluation of the respective quantities within the time interval

$$\begin{aligned} \ddot{\mathbf{d}}_\alpha &= (1-\alpha_M)\,\ddot{\mathbf{d}}_n + \alpha_M\ddot{\mathbf{d}}_{n+1} && (46)\\ \mathbf{R}_\alpha &= (1-\alpha_F)\,\mathbf{R}(\mathbf{d}_n) + \alpha_F\mathbf{R}(\mathbf{d}_{n+1}) && (47)\\ \mathbf{F}_\alpha &= (1-\alpha_F)\,\mathbf{F}(\mathbf{d}_n) + \alpha_F\mathbf{F}(\mathbf{d}_{n+1}) && (48) \end{aligned}$$

Substituting for the displacement and acceleration at time level $n+1$, the following system of equations is obtained

$$\begin{aligned} \alpha_M\frac{1}{\beta\Delta t^2}\mathbf{M}\mathbf{d}_{n+1} + \alpha_F\mathbf{R}(\mathbf{d}_{n+1}) - \alpha_F\mathbf{F}(\mathbf{d}_{n+1}) &= (1-\alpha_F)\mathbf{F}(\mathbf{d}_n) - (1-\alpha_F)\mathbf{R}(\mathbf{d}_n)\\ &\quad -(1-\alpha_M)\mathbf{M}\ddot{\mathbf{d}}_n + \alpha_M\mathbf{M}\left[\frac{1}{\beta\Delta t^2}\mathbf{d}_n + \frac{1}{\beta\Delta t}\dot{\mathbf{d}}_n + \left(\frac{1}{2\beta} - 1\right)\ddot{\mathbf{d}}_n\right] \end{aligned} \tag{49}$$

The resulting scheme is second order accurate and an appropriate selection of the involved time integration parameters allow for unconditional stable solutions of nonlinear dynamics. The classical Newmark method can be derived for $\alpha_M = \alpha_F = 1$.

2.7 Mesh deformation algorithm

A FSI algorithm requires a scheme for moving mesh vertices as the fluid-structure interfaces deform, rotate and translate. Several mesh deforming algorithms have been presented in the literature including the spring analogy [42], the elastic medium analogy [28], the edge swapping algorithm [43] and the remeshing algorithm [44]. These methods generally require solving discrete equations using iterative methods and the computational effort for these methods in three-dimension is not negligible. Therefore, we employ an alternative algebraic method [45] which assumes an exponential decay of the mesh displacement away from the fluid-structure interaction based on the minimum distance function. In addition, the equations of linear elasticity can be solved within the fluid domain and the robustness of the method can be further improved by modifying the Youngs module based on the distance function in order to increase the stiffness of small elements close to the fluid-structure interaction [46].

2.8 Coupled System of Equations

When the fluid and structure solvers are coupled with the interface conditions given in the section 2.3 and the mesh deformation algorithm described in the section 2.7, the following linear algebraic system of equations are obtained.

$$\left[\begin{array}{cc|c|cc|c} A_{uu} & A_{uu_\Gamma} & A_{up} & 0 & 0 & A_{uq} \\ 0 & A_{u_\Gamma u_\Gamma} & 0 & 0 & A_{ud_\Gamma} & 0 \\ \hline A_{pu} & A_{pu_\Gamma} & 0 & 0 & 0 & 0 \\ \hline 0 & 0 & 0 & A_{dd} & A_{dd_\Gamma} & 0 \\ A_{d_\Gamma u} & A_{d_\Gamma u_\Gamma} & A_{d_\Gamma p} & A_{d_\Gamma d} & A_{d_\Gamma d_\Gamma} & 0 \\ \hline 0 & 0 & 0 & 0 & A_{qd_\Gamma} & A_{qq} \end{array}\right] \left[\begin{array}{c} \mathbf{u} \\ \mathbf{u}_\Gamma \\ \hline p \\ \hline \mathbf{d} \\ \mathbf{d}_\Gamma \\ \hline \mathbf{q} \end{array}\right] = \left[\begin{array}{c} b_1 \\ 0 \\ \hline 0 \\ \hline b_4 \\ b_5 \\ \hline 0 \end{array}\right] \tag{50}$$

where Γ represents the variables at the common fluid-structure interface, $\mathbf{q}$ is the amount of mesh deformation within the fluid domain. These equations can be written as:

$$\begin{bmatrix} A_{uu} & A_{up} & A_{ud} & A_{uq} \\ A_{pu} & 0 & 0 & 0 \\ A_{du} & A_{dp} & A_{dd} & 0 \\ 0 & 0 & A_{qd} & A_{qq} \end{bmatrix} \begin{bmatrix} \mathbf{u} \\ p \\ \mathbf{d} \\ \mathbf{q} \end{bmatrix} = \begin{bmatrix} d_1 \\ 0 \\ d_3 \\ 0 \end{bmatrix} \tag{51}$$

In practice, the solution of equation (51) does not converge very quickly and it is rather difficult to construct robust preconditioners for the whole coupled system because of the zero-block diagonal resulting from the divergence-free constraint. In the present paper, we use an upper triangular right preconditioner which results in a scaled discrete Laplacian instead of a zero block in the original system. Then the modified system becomes

$$\begin{bmatrix} A_{uu} & A_{up} & A_{ud} & A_{uq} \\ A_{pu} & 0 & 0 & 0 \\ A_{du} & A_{dp} & A_{dd} & 0 \\ 0 & 0 & A_{qd} & A_{qq} \end{bmatrix} \begin{bmatrix} I & \hat{A}_{up} & 0 & 0 \\ 0 & I & 0 & 0 \\ 0 & 0 & I & 0 \\ 0 & 0 & 0 & I \end{bmatrix} = \begin{bmatrix} A_{uu} & A_{uu}\hat{A}_{up} + A_{up} & A_{ud} & A_{uq} \\ A_{pu} & A_{pu}\hat{A}_{up} & 0 & 0 \\ A_{du} & A_{du}\hat{A}_{up} + A_{dp} & A_{dd} & 0 \\ 0 & 0 & A_{qd} & A_{qq} \end{bmatrix} \tag{52}$$

and the zero block is replaced with $-A_{pu}A_{up}$, which is a scaled discrete Laplacian. Unfortunately, this leads to a significant increase in the number of non-zero elements due to the matrix-matrix multiplication. However, it is possible to replace the $-A_{up}$ block matrix in the upper triangular right preconditioner with a computationally less expensive matrix, $-\hat{A}_{up}$. The calculations indicate that the largest contribution for the pressure gradients in the momentum equations comes from the right and left elements that share the common edge/face where the components of the velocity vector are discretized. Therefore, we will use the contribution from these two elements for the $-\hat{A}_{up}$ matrix which leads maximum three non-zero entries per row. Although, this approximation does not change the convergence rate of an iterative solver significantly, it leads to a significant reduction in the computing time and memory requirement. The present one-level iterative solver is based on the restricted additive Schwarz method with the flexible GMRES(m) algorithm. Since the zero block is removed, a block-incomplete factorization coupled with the reverse Cuthill-McKee ordering [47] can be used within each partitioned sub-domains. The implementation of the preconditioned Krylov subspace algorithm and matrix-matrix multiplication were carried out using the PETSc [48] software package developed at the Argone National Laboratories. METIS library [49] is used to decompose the flow domain into a set of sub-domains.

3 NUMERICAL EXPERIMENTS

In this section, the proposed FSI algorithm described in Section 2 is validated for an unsteady Newtonian fluid interacting with an elastic rectangular bar behind a circular cylinder, a three-dimensional elastic solid confined in a rectangular channel and a pulsatile flow in a flexible tube, which mimics the case of pulsatile blood flow through elastic arteries.

3.1 Test Case I: Fluid–structure interaction of an elastic bar behind a rigid cylinder

The first case corresponds to the FSI benchmark problem proposed by Hron and Turek [50]. The problem consists of an elastic bar behind a rigid circular cylinder which is placed asymmetrically between parallel lateral walls as shown in Figure 2.

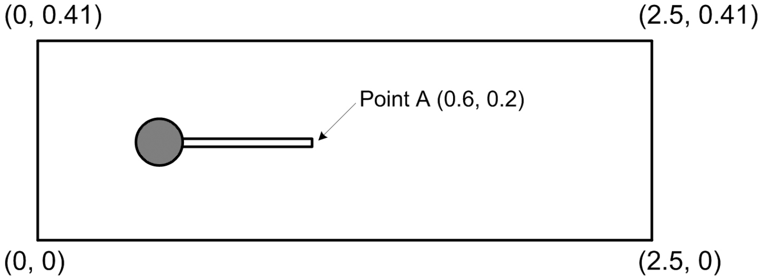

Figure 2: The geometric description of the first validation case.

The parameters $H = 0.41$ is the 2D channel height, $L = 2.5$ is the channel length, $D = 0.1$ is the cylinder diameter, $l = 0.35$ is the bar length and $h = 0.02$ is the bar height. The cylinder is positioned at (0.2,0.2) from the left bottom corner of the channel. The control point A is attached to the structure and moving in time starting from (0.6,0.2). The inflow velocity is set to

$$u(y) = 1.5\langle U\rangle \frac{y(H-y)}{(H/2)}^2 = 1.5\langle U\rangle \frac{4.0}{0.1681} y(0.41-y) \tag{53}$$

where $\langle U\rangle$ is the mean inflow velocity. The outlet boundary conditions are set to natural (traction-free) boundary conditions:

$$\frac{\partial u}{\partial x} = p, \qquad \frac{\partial v}{\partial x} = 0 \tag{54}$$

Table 1: Fluid and structure properties for Test Case I

		FSI1	FSI2
Fluid	Density ρ_f	1000	1000
	Dynamic viscosity μ_f	1×10^{-3}	1×10^{-3}
	Mean Inflow velocity $\langle U \rangle$	0.2	2
Solid	Density ρ_s	1000	1000
	Poisson ratio ν_s	0.4	0.4
	Shear modulus μ_s	0.5×10^6	2×10^6

Table 2: Displacements at point A for FSI1 of Test Case I. $Re = 20$.

	DOF	$d_x\ [\times 10^{-3}]$	$d_y\ [\times 10^{-3}]$
Present FSI solver	$375,216$	0.022387	0.81408
Hron and Turek [50]	$304,128$	0.022732	0.82071
Degroote et al. [52]	$320,372$	0.022651	0.83478
Richter and Wick [53]	$351,720$	0.022695	0.81556

We consider two cases with two different inflow speeds and shear moduli for this test problem with the physical parameters indicated in Table 1. FSI1, where the Reynolds number $Re = 20$, results in a steady state solution, while FSI2, which corresponds to FSI3 of Hron and Turek [50], results in an unsteady flow solution with the Reynolds number $Re = 200$. For the present test case, we use an unstructured mesh with $78,921$ quadrilateral elements and $79,806$ nodes, which result in a total of 375,216 DOF for the whole domain. The mesh is highly refined close to the solid surfaces using local mesh refinement algorithms within the CUBIT [51] library. The computed $u-$velocity vector components for FSI2 are shown in Figure 3 with the streamlines at different time levels. The streamlines indicate an alternating large recirculation zone just behind the cylinder. The time variation of vertical displacement for FSI2 at point $A(0.6, 0.2)$ on the tip of the bar is given in Figure 4. The computed deformations at point A for the steady and the unsteady flow solutions are tabulated in Table 2 and 3 with comparisons to the computations from different authors. The present results are in relative good agreement with the results in the literature and the present calculations can correctly predict the amplitude of the oscillations for the unsteady flow solution (FSI2). The period of oscillations for the elastic structure is about $0.1805\ s$. The motion of the structure and the corresponding displacements of the reference point are illustrated in Figure 5 for one complete cycle.

3.2 Test Case II: 3D FSI problem of an elastic beam in a cross flow

In the second example, the present FSI solver is validated for a 3-dimensional stationary problem, where an elastic beam is immersed in a rectangular channel as illustrated in Figure 6. The dimensions of the channel is $[0, 1.5] \times [0, 0.4] \times [-0.4, 0.4]$ while the dimensions of solid domain is $[0.4, 0, 5] \times [0, 0.2] \times [-0.2, 0.2]$. The problem is considered to be symmetric in the $xy-$plane. The present problem is solved by Richter [56] using a variational monolithic Ar-

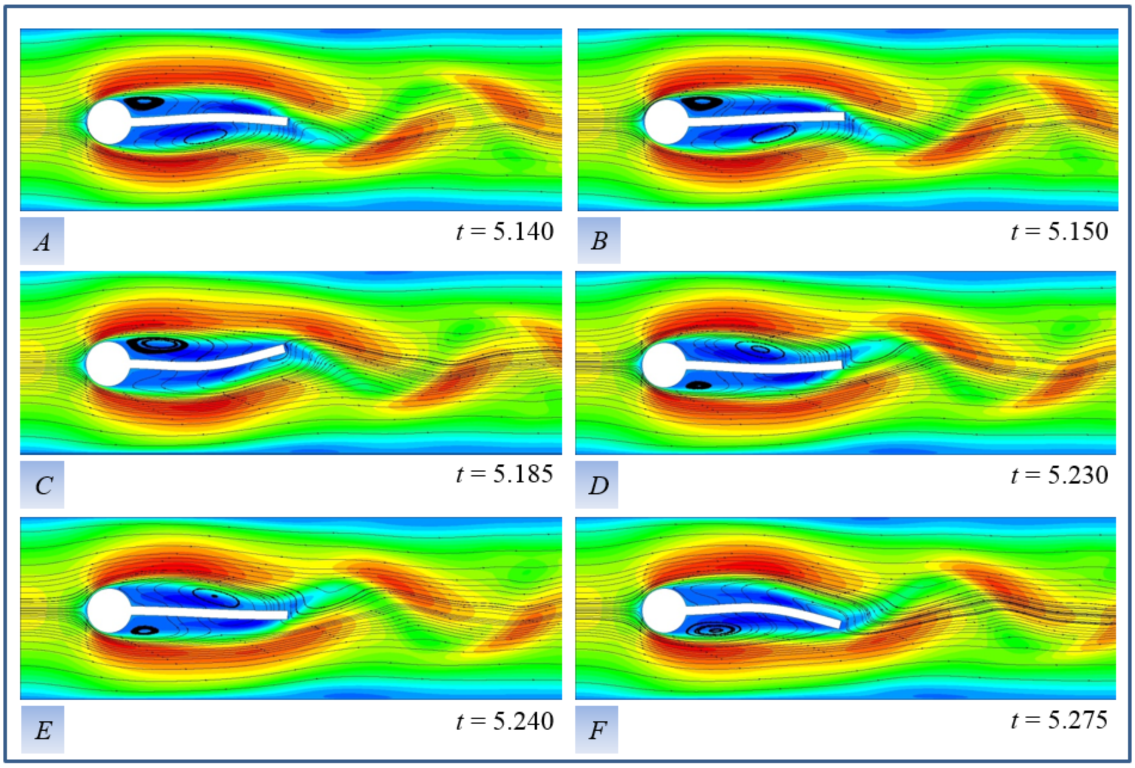

Figure 3: The computed $u-$velocity vector component contours with the streamlines for an elastic bar behind a rigid cylinder at $Re = 200$.

Table 3: Displacements at point A for FSI2 of Test Case I. $Re = 200$.

	DOF	d_x $[\times 10^{-3}]$	d_y $[\times 10^{-3}]$
Present FSI solver	$375,216$	-2.521 ± 2.655	$+1.327 \pm 33.659$
Hron and Turek [50]	$304,128$	-2.69 ± 2.53	$+1.48 \pm 34.38$
Wick [54]	$72,696$	-2.84 ± 2.67	$+1.28 \pm 34.61$
Chabannes et al. [55]	$86,256$	-2.90 ± 2.77	$+1.33 \pm 34.90$

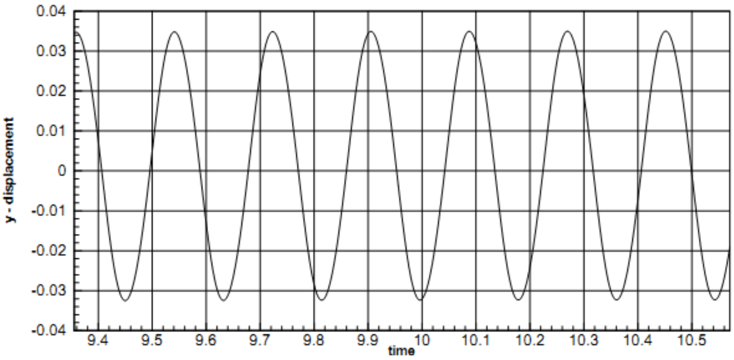

Figure 4: The time variation of vertical displacement for an elastic bar behind a rigid cylinder at $Re = 200$.

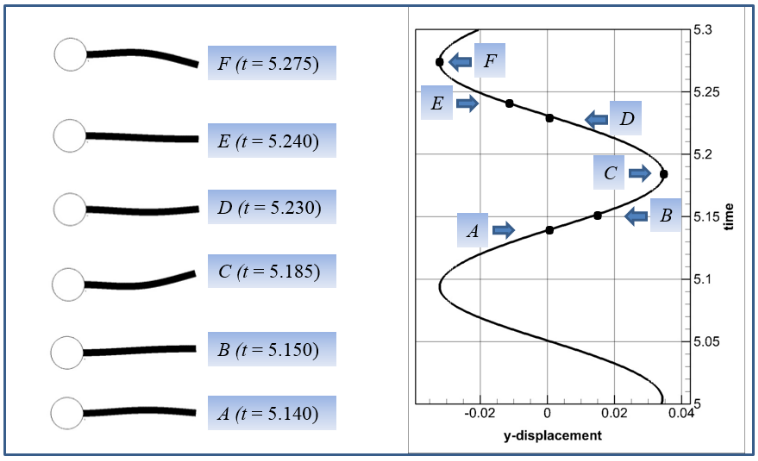

Figure 5: The motion of the elastic bar at $Re = 200$ for one complete cycle.

bitrary Lagrangian Eulerian formulation with local mesh refinement, resulting upto $7,600,775$ DOF. The author provides the structure displacement values in $x-$ and $y-$direction at the point $A(0.45, 0.15, 0.15)$ and the drag forces on the solid body. The inlet velocity has a parabolic distribution given

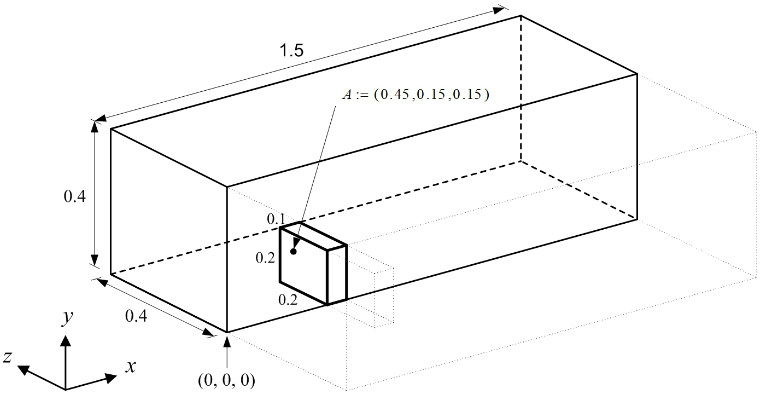

Figure 6: The geometry for 3D FSI problem.

$$u(y,z) = \frac{0.3}{0.2^2 \times 0.4^2} y\,(0.4 - y)\left(0.4^2 - z^2\right) \tag{55}$$

with the maximum value of $u_{max} = 0.3$. The outlet boundary conditions are set to natural (traction-free) boundary conditions.

The Reynolds number is based on an average inflow velocity ($\langle U \rangle = 0.2$) and an obstacle of height $h = 0.2$ and its value is $Re = 40$. The properties for the fluid and the solid are tabulated in Table 4. The computational mesh consists of $362,224$ hexahedral elements and $374,523$ vertices leading to $4,096,6514$ DOF. The mesh is initially constructed from a Cartesian mesh and then two levels of refinement are performed near the solid walls. The computed $u-$velocity vector component isosurfaces with the streamtraces are shown in Figure 7 at $Re = 40$. In addition, the streamtraces computed on the solid walls are shown in Figure 8 on the front and on the back side of the solid body. The computed deformation vector components at the point $A(0.45, 0.15, 0.15)$ are given in Table 5 for more precise comparison and the values are compared with the results of Richter [56]. The results are relatively in good agreement.

Table 4: Fluid and structure properties for test case II

Fluid		Structure	
Density	$\rho_f = 1000$	Density	$\rho_s = 1000$
Kinematic viscosity	$\nu_f = 10^{-3}$	Poisson ratio	$\nu_s = 0.4$
Average Inflow velocity	$\langle U \rangle = 0.2$	Shear Modulus	$\mu_s = 5 \times 10^5$

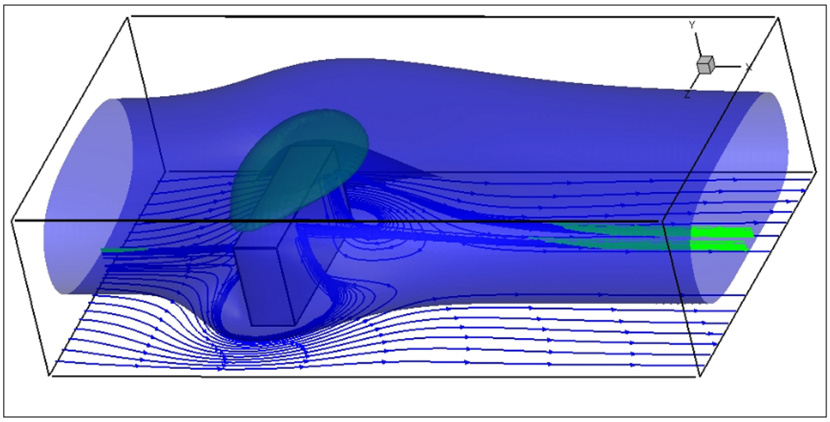

Figure 7: The computed $u-$velocity vector component isosurfaces with the streamtraces for an elastic bar confined in a rectangular channel at $Re = 40$.

Table 5: Displacement at point A for Test Case II

	Present FSI solver	Richter [56]
DOF	$4,096,651$	$7,600,775$
Δx	5.753204×10^{-5}	5.9280×10^{-5}
Δy	8.735848×10^{-7}	-
Δz	8.533534×10^{-7}	-

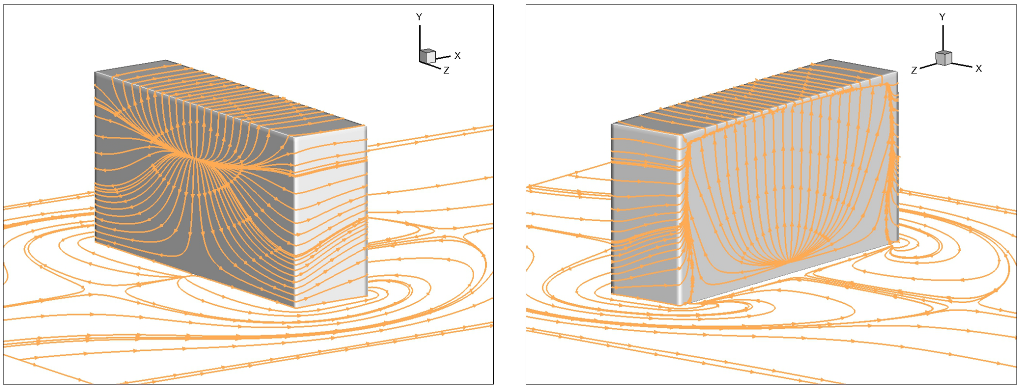

(a) Upwind Direction (b) Downwind Direction

Figure 8: The computed streamtraces on the solid walls for an elastic bar confined in a rectangular channel at $Re = 40$.

3.3 Test Case III: Pressure-pulse in a flexible tube

In the last example we consider a three-dimensional dynamic FSI benchmark problem proposed by [57], which has been considered by many authors [58, 59, 20]. The problem is related to the blood flow through elastic arteries and the test configuration consists of an incompressible viscous flow through a flexible circular tube with an inner radius of $0.5\,cm$ and a wall thickness of $0.1\,cm$. The tube wall is clamped at both ends and a pressure boundary condition is imposed on the fluid at the inflow and outflow boundaries. The fluid is initially at rest and a pressure of $1.3332 \times 10^{-4}\ dyn/cm^2$ is imposed on the inflow boundary for $t < 0.003\,s$, while at the outflow boundary, the pressure is set to zero throughout the analysis. The physical properties for the Saint Venant-Kirchhoff material and the Newtonian fluid used for the third test case are listed in Table 6. The mesh for this test case consists of $148,480$ hexahedral elements and $154,305$ vertices for the whole computational domain. Throughout the computations, the time step is set to 1×10^{-4}. In Figure 9, the time variations of the radial components of displacement and velocity of the inner tube wall at half the length of the pipe are presented for the first $0.02s$ of motion. The snapshot of the computed deformation contours at $0.0069s$ is given in Figure 10, which is comparable with the structural deformation result presented in [20]. It should be noted that the wall deformation presented in Figure 10 are exaggerated by a factor of 10 for clarity. In the future, we will repeat the same problem with the second-order backward difference in the fluid domain.

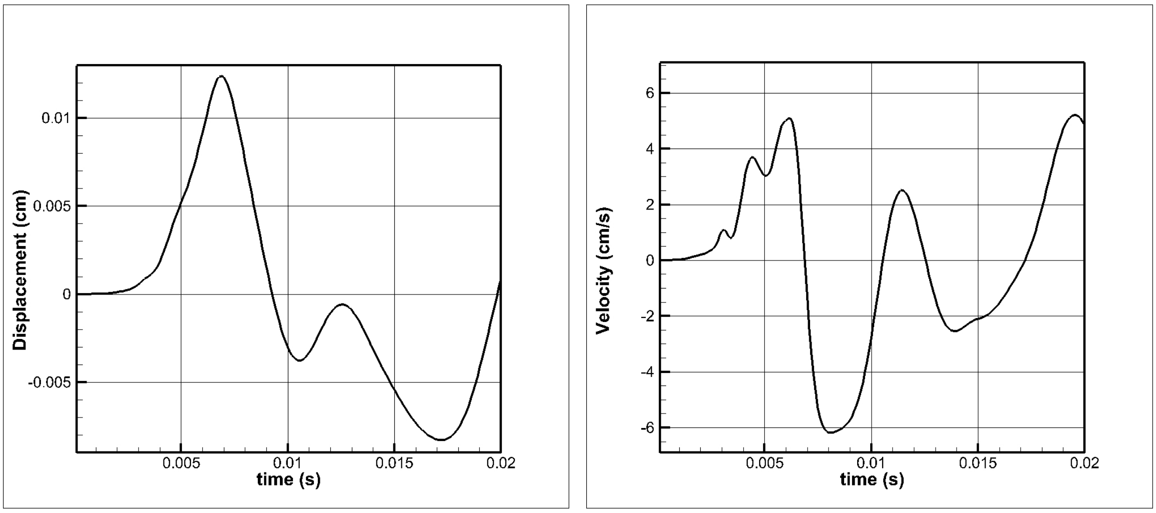

(a) Displacement

(b) Velocity

Figure 9: Radial components of displacement and velocity of the inner tube wall at half the length of the pipe.

Table 6: Fluid and structure properties for test case III

Fluid		Structure	
Density	$\rho_f = 1\,g/cm^3$	Density	$\rho_s = 1.2\,g/cm^3$
Dynamic viscosity	$\mu_f = 3 \times 10^{-2}\,g/cm \cdot s$	Poisson ratio	$\nu_s = 0.3$
		Young modulus	$E_s = 3 \times 10^6$

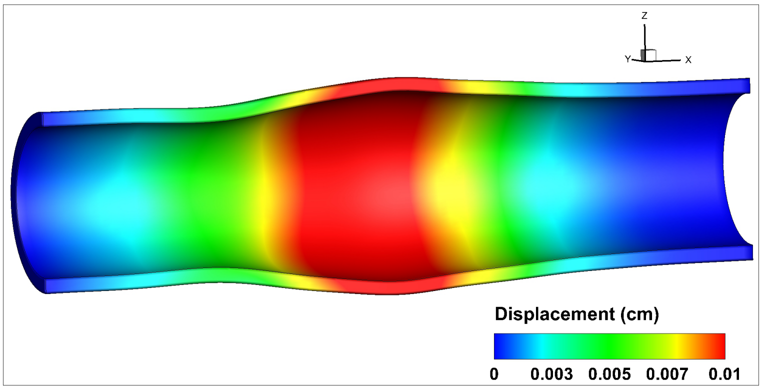

Figure 10: The computed radial displacement contours at $t = 0.0069s$. The wall deformation are exaggerated by a factor of 10 for clarity.

4 CONCLUSIONS

A new algorithm based on the ALE formulation is presented for a fully coupled solution of the large-scale FSI problems where the fluid is modeled by the incompressible Navier-Stokes equations and the structure is modeled by the St. Venant-Kirchhoff model. The present ALE formulation does not require any *ad-hoc* modifications in order to enhance the pressure-velocity coupling. The continuity equation is satisfied within each element exactly and the summation of the continuity equations can be exactly reduced to the domain boundary, which is important for the global mass conservation. A special attention is also given to satisfy the Geometric Conservation Law (GCL) on moving meshes at discrete level. The deformation of the solid domain is governed by the constitutive laws for the nonlinear Saint Venant-Kirchhoff material and the classical Galerkin finite element is used to discretize the governing equations in a Lagrangian frame. The implementation of the preconditioned coupled iterative solvers is based on the PETSc library for improving the efficiency of the parallel code. The present numerical algorithm is validated for a Newtonian fluid interacting with an elastic rectangular bar behind a circular cylinder, a three-dimensional elastic solid confined in a rectangular channel and a pulsatile flow in a flexible tube, which mimics the case of pulsatile blood flow through elastic arteries.

5 ACKNOWLEDGMENTS

The authors acknowledge financial support from Turkish National Scientific and Technical Research Council (TUBITAK) through project number 112M107. The authors also gratefully acknowledge the use of the Chimera machine at the Faculty of Aeronautics and Astronautics at ITU, the computing resources provided by the National Center for High Performance Computing of Turkey (UYBHM) under grant number 10752009 and the computing facilities at TUBITAK ULAKBIM, High Performance and Grid Computing Center.

REFERENCES

[1] X. Zhao, Y. Zhu, and S. Zhang, “Transonic wing flutter predictions by a loosely-coupled method,” *Computers & Fluids*, vol. 58, no. 0, pp. 45 – 62, 2012.

[2] X. Chen, G.-C. Zha, and M.-T. Yang, “Numerical simulation of 3-d wing flutter with fully coupled fluidstructural interaction,” *Computers & Fluids*, vol. 36, no. 5, pp. 856 – 867,

2007.

[3] Y.-J. Lee, Y.-T. Jhan, and C.-H. Chung, "Fluidstructure interaction of frp wind turbine blades under aerodynamic effect," *Composites Part B: Engineering*, vol. 43, no. 5, pp. 2180 – 2191, 2012.

[4] E. Sheta and L. Huttsell, "Characteristics of f/a-18 vertical tail buffeting," *Journal of Fluids and Structures*, vol. 17, no. 3, pp. 461 – 477, 2003.

[5] S. Sathe, R. Benney, R. Charles, E. Doucette, J. Miletti, M. Senga, K. Stein, and T. Tezduyar, "Fluidstructure interaction modeling of complex parachute designs with the spacetime finite element techniques," *Computers & Fluids*, vol. 36, no. 1, pp. 127 – 135, 2007.

[6] W. Sinz and S. Hermann, "The development of a 3d-navierstokes code for the simulation of an airbag inflation," *Simulation Modelling Practice and Theory*, vol. 16, no. 8, pp. 885 – 899, 2008.

[7] B. Augier, P. Bot, F. Hauville, and M. Durand, "Experimental validation of unsteady models for fluid structure interaction: Application to yacht sails and rigs," *Journal of Wind Engineering and Industrial Aerodynamics*, vol. 101, no. 0, pp. 53 – 66, 2012.

[8] M. Glück and M. Breuer and F. Durst and A. Halfmann and E. Rank, "Computation of fluidstructure interaction on lightweight structures," *Journal of Wind Engineering and Industrial Aerodynamics*, vol. 89, no. 1415, pp. 1351 – 1368, 2001.

[9] H. Zhang, L. Liu, M. Dong, and H. Sun, "Analysis of wind-induced vibration of fluid-structure interaction system for isolated aqueduct bridge," *Engineering Structures*, vol. 46, no. 0, pp. 28 – 37, 2013.

[10] A. L. Braun and A. M. Awruch, "Aerodynamic and aeroelastic analyses on the caarc standard tall building model using numerical simulation," *Computers & Structures*, vol. 87, no. 910, pp. 564 – 581, 2009.

[11] X. Yang, Y. Liu, and J. Yang, "Fluid-structure interaction in a pulmonary arterial bifurcation," *Journal of Biomechanics*, vol. 40, no. 12, pp. 2694 – 2699, 2007.

[12] J. D. Hart, F. Baaijens, G. Peters, and P. Schreurs, "A computational fluid-structure interaction analysis of a fiber-reinforced stentless aortic valve," *Journal of Biomechanics*, vol. 36, no. 5, pp. 699 – 712, 2003.

[13] T. B. Le and F. Sotiropoulos, "Fluidstructure interaction of an aortic heart valve prosthesis driven by an animated anatomic left ventricle," *Journal of Computational Physics*, no. 0, pp. –, 2012.

[14] D. Alizadehrad, Y. Imai, K. Nakaaki, T. Ishikawa, and T. Yamaguchi, "Quantification of red blood cell deformation at high-hematocrit blood flow in microvessels," *Journal of Biomechanics*, vol. 45, no. 15, pp. 2684 – 2689, 2012.

[15] Y. Liu and W. K. Liu, "Rheology of red blood cell aggregation by computer simulation," *Journal of Computational Physics*, vol. 220, no. 1, pp. 139 – 154, 2006.

[16] K. C. Park, C. A. Felippa, and J. A. Deruntz, "Stabilization of staggered solution procedures for fluid-structure interaction analysis," in *Computational Methods for Fluid-Structure Interaction Problems* (T. Belytschko and T. L. Geers, eds.), pp. 94–124, ASME, 1977.

[17] H. G. Matthies and J. Steindorf, "Partitioned strong coupling algorithms for fluidstructure interaction," *Computers & Structures*, vol. 81, no. 811, pp. 805 – 812, 2003.

[18] J. Degroote and J. Vierendeels, "Multi-solver algorithms for the partitioned simulation of fluidstructure interaction," *Computer Methods in Applied Mechanics and Engineering*, vol. 200, no. 2528, pp. 2195 – 2210, 2011.

[19] F. J. Blom, "A monolithical fluid-structure interaction algorithm applied to the piston problem," *Computer Methods in Applied Mechanics and Engineering*, vol. 167, no. 34, pp. 369 – 391, 1998.

[20] M. W. Gee, U. Kttler, and W. A. Wall, "Truly monolithic algebraic multigrid for fluidstructure interaction," *International Journal for Numerical Methods in Engineering*, vol. 85, no. 8, pp. 987–1016, 2011.

[21] R. L. Muddle, M. Mihajlovic, and M. Heil, "An efficient preconditioner for monolithically-coupled large-displacement fluid-structure interaction problems with pseudo-solid mesh updates," *Journal of Computational Physics*, vol. 231, no. 21, pp. 7315 – 7334, 2012.

[22] J. Janela, A. Moura, and A. Sequeira, "A 3d non-newtonian fluidstructure interaction model for blood flow in arteries," *Journal of Computational and Applied Mathematics*, vol. 234, no. 9, pp. 2783 – 2791, 2010.

[23] F. Nobile, "Coupling strategies for the numerical simulation of blood flow in deformable arteries by 3d and 1d models," *Mathematical and Computer Modelling*, vol. 49, no. 1112, pp. 2152 – 2160, 2009.

[24] C. Förster, W. A. Wall, and E. Ramm, "Artificial added mass instabilities in sequential staggered coupling of nonlinear structures and incompressible viscous flows," *Computer Methods in Applied Mechanics and Engineering*, vol. 196, no. 7, pp. 1278 – 1293, 2007.

[25] M. Heil, A. L. Hazel, and J. Boyle, "Solvers for large-displacement fluid structure interaction problems: segregated versus monolithic approaches," *Computational Mechanics*, vol. 43, pp. 91–101, Dec. 2008.

[26] U. Küttler, M. Gee, C. Förster, A. Comerford, and W. A. Wall, "Coupling strategies for biomedical fluidstructure interaction problems," *International Journal for Numerical Methods in Biomedical Engineering*, vol. 26, no. 3-4, pp. 305–321, 2010.

[27] M. Behr and T. E. Tezduyar, "Finite element solution strategies for large-scale flow simulations," *Computer Methods in Applied Mechanics and Engineering*, vol. 112, no. 14, pp. 3–24, 1994.

[28] A. Johnson and T. Tezduyar, "Mesh update strategies in parallel finite element computations of flow problems with moving boundaries and interfaces," *Computer Methods in Applied Mechanics and Engineering*, vol. 119, no. 12, pp. 73 – 94, 1994.

[29] A. T. Barker and X.-C. Cai, "Scalable parallel methods for monolithic coupling in fluid-structure interaction with application to blood flow modeling," *Journal of Computational Physics*, vol. 229, pp. 642–659, Feb. 2010.

[30] C. Hirt, A. Amsden, and J. Cook, "An arbitrary lagrangian-eulerian computing method for all flow speeds," *Journal of Computational Physics*, vol. 14, no. 3, pp. 227 – 253, 1974.

[31] P. D. Thomas and C. K. Lombard, "Geometric Conservation Law and Its Application to Flow Computations on Moving Grids," *AIAA Journal*, vol. 17, pp. 1030–1037, Oct. 1979.

[32] T. J. Hughes, W. K. Liu, and T. K. Zimmermann, "Lagrangian-eulerian finite element formulation for incompressible viscous flows," *Computer Methods in Applied Mechanics and Engineering*, vol. 29, no. 3, pp. 329 – 349, 1981.

[33] J. Donea, S. Giuliani, and J. Halleux, "An arbitrary lagrangian-eulerian finite element method for transient dynamic fluid-structure interactions," *Computer Methods in Applied Mechanics and Engineering*, vol. 33, no. 13, pp. 689 – 723, 1982.

[34] Y.-H. Hwang, "Calculations of Incompressible Flow on a Staggered Triangular Grid, Part I: Mathematical Formulation," *Numerical Heat Transfer Part B - Fundamentals*, vol. 27, pp. 323–336, Apr. 1995.

[35] S. Rida, F. McKenty, F. L. Meng, and M. Reggio, "A staggered control volume scheme for unstructured triangular grids," *International Journal for Numerical Methods in Fluids*, vol. 25, pp. 697–717, Sept. 1997.

[36] F. H. Harlow and J. E. Welch, "Numerical Calculation of Time-Dependent Viscous Incompressible Flow of Fluid with Free Surface," *Physics of Fluids*, vol. 8, pp. 2182–2189, Dec. 1965.

[37] C. Farhat, *CFD-Based Nonlinear Computational Aeroelasticity*. John Wiley & Sons, Ltd, 2004.

[38] N. M. Newmark, "A method of computation for structural dynamics," *Journal of the Engineering Mechanics Division*, vol. 85, no. 3, pp. 67–94, 1959.

[39] J. Chung and G. M. Hulbert, "A Time Integration Algorithm for Structural Dynamics With Improved Numerical Dissipation: The Generalized-α Method," *Journal of Applied Mechanics*, vol. 60, p. 371, 1993.

[40] W. K. Anderson and D. L. Bonhaus, "An implicit upwind algorithm for computing turbulent flows on unstructured grids," *Computers & Fluids*, vol. 23, no. 1, pp. 1–21, 1994.

[41] B. Timothy, *A 3-D upwind Euler solver for unstructured meshes*. Meeting Paper Archive, American Institute of Aeronautics and Astronautics, 1963. doi:10.2514/6.1991-1548.

[42] J. T. Batina, "Unsteady euler airfoil solutions using unstructured dynamic meshes," *AIAA Journal*, vol. 28, no. 8, pp. 1381–1388, 1990.

[43] M. Dai and D. P. Schmidt, "Adaptive tetrahedral meshing in free-surface flow," *Journal of Computational Physics*, vol. 208, no. 1, pp. 228 – 252, 2005.

[44] A. A. Johnson and T. E. Tezduyar, "Advanced mesh generation and update methods for 3d flow simulations," *Computational Mechanics*, vol. 23, pp. 130–143, 1999.

[45] T. Gerhold and J. Neumann, *The Parallel Mesh Deformation of the DLR TAU-Code*, vol. 96 of *Notes on Numerical Fluid Mechanics and Multidisciplinary Design (NNFM)*, ch. 20, pp. 162–169. Springer Berlin Heidelberg, 2008.

[46] M. Sahin and K. Mohseni, "An arbitrary lagrangianeulerian formulation for the numerical simulation of flow patterns generated by the hydromedusa aequorea victoria," *Journal of Computational Physics*, vol. 228, no. 12, pp. 4588 – 4605, 2009.

[47] E. Cuthill and J. McKee, "Reducing the bandwidth of sparse symmetric matrices," in *Proceedings of the 1969 24th national conference*, ACM '69, (New York, NY, USA), pp. 157 – 172, ACM, 1969.

[48] S. Balay, J. Brown, , K. Buschelman, V. Eijkhout, W. D. Gropp, D. Kaushik, M. G. Knepley, L. C. McInnes, B. F. Smith, and H. Zhang, "PETSc users manual," Tech. Rep. ANL-95/11 - Revision 3.3, Argonne National Laboratory, 2012.

[49] G. Karypis and V. Kumar, "A fast and high quality multilevel scheme for partitioning irregular graphs," *SIAM Journal on Scientific Computing*, vol. 20, no. 1, pp. 359–392, 1999.

[50] S. Turek and J. Hron, "Proposal for numerical benchmarking of fluid-structure interaction between an elastic object and laminar incompressible flow," in *Fluid-Structure Interaction* (H.-J. Bungartz and M. Schfer, eds.), vol. 53 of *Lecture Notes in Computational Science and Engineering*, pp. 371–385, Springer Berlin Heidelberg, 2006.

[51] T. D. Blacker, S. Benzley, S. Jankovich, R. Kerr, J. Kraftcheck, R. Kerr, P. Knupp, R. Leland, D. Melander, R. Meyers, S. Mitchell, J. Shepard, T. Tautges, and D. White, "Cubit mesh generation enviroment users manual volume 1," tech. rep., Albuquerque, NM.

[52] J. Degroote, R. Haelterman, S. Annerel, P. Bruggeman, and J. Vierendeels, "Performance of partitioned procedures in fluidstructure interaction," *Computers & Structures*, vol. 88, no. 78, pp. 446 – 457, 2010.

[53] T. Richter and T. Wick, "Finite elements for fluidstructure interaction in ale and fully eulerian coordinates," *Computer Methods in Applied Mechanics and Engineering*, vol. 199, no. 4144, pp. 2633 – 2642, 2010.

[54] T. Wick, "Solving monolithic fluid-structure interaction problems in arbitrary lagrangian eulerian coordinates with the deal.ii library," tech. rep., University of Heidelberg, 2011.

[55] V. Chabannes, G. Pena, and C. Prud'Homme, "High order fluid structure interaction in 2D and 3D. Application to blood flow in arteries." Submitted to Elsevier Journal of Computational and Applied Mathematics (JCAM), Feb. 2012.

[56] T. Richter, "Goal-oriented error estimation for fluidstructure interaction problems," *Computer Methods in Applied Mechanics and Engineering*, vol. 223-224, no. 0, pp. 28 – 42, 2012.

[57] J.-F. Gerbeau and M. Vidrascu, “A quasi-newton algorithm based on a reduced model for fluid-structure interaction problems in blood flows,” *ESAIM: Mathematical Modelling and Numerical Analysis*, vol. 37, pp. 631–647, 6 2003.

[58] U. Küttler and W. A. Wall, “Fixed-point fluidstructure interaction solvers with dynamic relaxation,” *Computational Mechanics*, vol. 43, pp. 61–72, 2008.

[59] A. Malan and O. Oxtoby, “An accelerated, fully-coupled, parallel 3d hybrid finite-volume fluidstructure interaction scheme,” *Computer Methods in Applied Mechanics and Engineering*, vol. 253, no. 0, pp. 426 – 438, 2013.